Available online at www.sciencedirect.com
SCIENCE DIRECT
aquacultural engineering
Aquacultural Engineering 33 (2005) 285–303
www.elsevier.com/locate/aqua-online

Numerical modeling and design of inflatable structures—application to open-ocean-aquaculture cages☆

Jeffrey D. Suhey [a,1], Nam H. Kim [a,*], Christopher Niezrecki [b,2]

[a] *Department of Mechanical and Aerospace Engineering, University of Florida, POB 116250, Gainesville 326116250, FL 32611, USA*
[b] *Department of Mechanical Engineering, University of Massachusetts Lowell, Lowell, MA 01854, USA*

Received 16 October 2004; accepted 13 March 2005

Abstract

Numerical simulation and design of an inflatable open-ocean-aquaculture cage is presented using nonlinear finite element analysis of membrane structures. Numerical instability caused by the tension-only membrane has been removed by adding an artificial shell with small stiffness. The material properties of a fabric material are obtained from tensile tests in both hoop and longitudinal directions, assuming the material is anisotropic. Wrinkling, defined as an onset of compressive stress, is monitored as design criteria. The finite element model is validated using a modified beam theory for the inflatable structure by comparing the maximum deflection and stress. Good agreement is observed between the numerical and theoretical results. A full-scale cage model is created using membrane, shell, and string elements to test the stiffness and integrity of the system. The feasibility study indicates that the inflated structure has sufficient stiffness to be used as the structural support within a fish cage. Based on the parameter study, several designs are suggested.

Keywords: Open-ocean-aquaculture cages; Inflatable structure; Finite element analysis; Parameter study

☆ This work is currently ''patent pending''.

* Corresponding author. Tel.: +1 352 846 0665; fax: +1 352 392 7303.
E-mail addresses: nkim@ufl.edu (N.H. Kim), chris_niezrecki@uml.edu (C. Niezrecki).
[1] Present address: United Space Alliance, Merritt Island, FL, USA.
[2] Tel.: +1 978 934 2963.

0144-8609/$ – see front matter
doi:10.1016/j.aquaeng.2005.03.001

1. Introduction

The ever increasing demands of the world population on ocean resources have resulted in severe over-fishing in many parts of the world. Without supplementation through aquaculture, world-wide fisheries production will be unable to meet the needs of the growing human population. In particular, open-ocean-aquaculture (OOA) is one area that shows great promise to meet the needs of the US markets and reduce the need to import fish from abroad (Bucklin and Howell, 1998). It is also believed that OOA has the potential to have a significant impact within the waters of Florida, the Atlantic coast, the Gulf of Mexico, and the Caribbean Sea (Davis et al., 1998; Bridger et al., 2001).

Current OOA cage design falls in one of the four general categories. Class 1 cages rely on buoyancy and gravitational forces to maintain their shape and are typically referred to as gravity cages. Class 2 cages are anchor tensioned while class 3 cages are self-supporting cages that resist net deformation due to a combination of tension in the flexible members and compression in the rigid members. These structures are referred to as ''tensegrity'' structures. Lastly, class 4 cages are rigid self-supporting structures typically constructed from beams and jointed members (Loverich and Forster, 2000). A variety of different types of cages are commercially available (Bridgestone, Polar Cirkel, Farm Ocean, Sadco-Shelf, Ocean Spar Technologies, L.L.C., etc.) however the Sea Station® Cage (class 3) has become increasingly popular and can be considered the state-of-the-art in OOA cage designs.

Inflatable structures have been used in many civil and aerospace applications, however they have not been considered for use underwater. The use of inflatables has the potential to advance cage design and to resolve some of the issues that hold back the open ocean aquaculture community. Lightweight inflatables may greatly decrease the cost of cage transportation, deployment, assembly, and maintenance. A semi-rigid, inflatable, tensegrity-structure design, maintains divergence volume, which is critical for fish health and aquaculture success. The inflated cage retains the system integrity by using pressurized water instead of air.

Fig. 1 shows the basic layout, including a rigid central spar and surrounding ring, typical of a class 3 cage design (Loverich and Forster, 2000). In this paper, the class 3 cage design is modified by replacing the rigid components with inflated members. This creates a lightweight, semi-rigid, and deployable structure. The objective of this paper is to determine the feasibility of an aquaculture cage design based on flexible pressurized members. The focus is on the stiffness of the water-filled inflatables and system integrity.

Several research results are available for analyzing an inflatable-membrane structure subject to bending, including a (1) nonlinear approach (Douglas, 1969), (2) linear shell method using continuum mechanics (Topping, 1964; Jenkins, 2001), (3) finite element analysis approach (Sakamoto et al., 2001), and (4) modified conventional beam theory (Comer and Levy, 1963; Main et al., 1994, 1995). However, the above-referenced approaches are limited to a simple beam-type structure, rather than complex engineering systems. Thus, it is necessary to develop an analysis capability that can estimate system integrity and can be applied to a system design.

In this paper, a finite element approach is chosen as a simulation and design tool because of its ease of modeling complex geometries and ability to provide a visualization

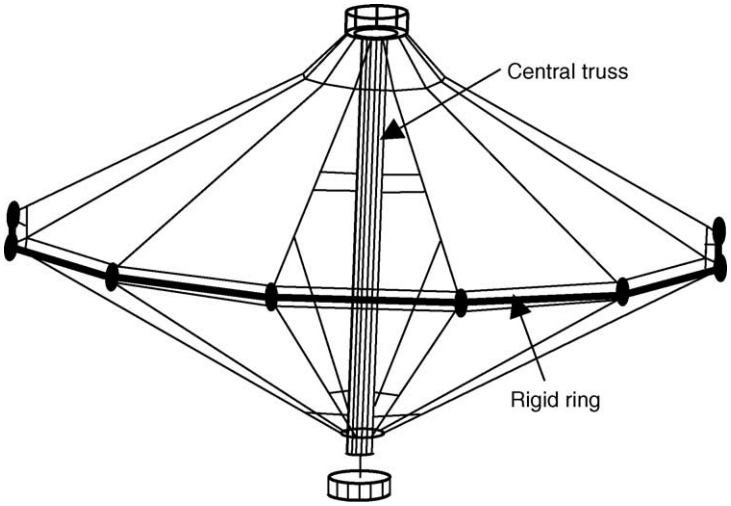

Fig. 1. Example of a class 3 cage design (Loverich and Forster, 2000).

of the deformed behavior (Bathe, 1996). Nonlinear elements are used to model the tension-only behavior of the fabric material. A modified beam theory for the inflatable structure is adapted to apply appropriate loads and boundary conditions within the model. The finite element solution is verified with the behavior of a theoretical modified beam analysis.

The paper is structured as follows. Section 2 reviews the theory for an inflatable beam. The comparison of the finite element model with the theoretical results is performed in Section 3. In Section 4, results are presented on the measured material properties using tensile tests in the hoop and longitudinal directions. Section 5 explains finite element modeling of the cage structure and Section 6 presents the results and observations of the simulation. These are followed by conclusions in Section 7.

2. Modified beam theory for inflatable structures

In this section, the modified conventional beam theory (Main et al., 1994, 1995) is summarized in order to verify the finite element model. The goal is to calculate the magnitudes of deflection and stress at the onset of wrinkling. The model used within the derivation is an internally pressurized circular-cylindrical, closed-end fabric tube. The essence of the inflatable theory is a representative pretension force that replaces the internal pressure acting on the caps in the analysis. This pretension force creates a stress that opposes the compressive bending stress and adds to the bending tensile stress. Wrinkling occurs when the compressive portion of bending stress exceeds the pretension stress. Fig. 2 shows the pretension stress distribution in a model beam subject to bending.

In thin structures, resultant properties are often used by integrating over the thickness. Let I^* be the resultant area moment of inertia of a circular tube and E^* is the resultant

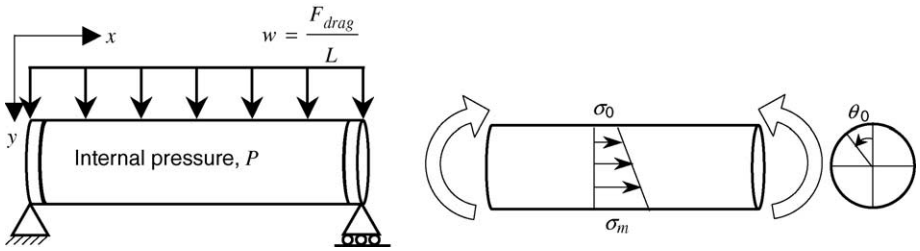

Fig. 2. Simply-supported boundary conditions supporting a beam model subject to distributed force drag loading.

elastic modulus. The governing equation for the traditional beam bending problem is given by:

$$\frac{\mathrm{d}^2 y}{\mathrm{d}x^2} = \frac{M(x)}{E^* I^*}, \tag{1}$$

where $I^* = \pi r^3$. The above equation can be integrated to determine deflection, y, for the pinned-roller boundary conditions as shown in Fig. 2, as:

$$y = \frac{w}{24E^*\pi r^3}(2Lx^3 - x^4 - L^3 x). \tag{2}$$

Consider a pressurized tube, as illustrated in Fig. 2, under a distributed load. For the cage structure, water currents would impart a similar distributed load on the relevant members. In the conventional beam theory, the transverse load creates bending stress that is linear across the cross-section. Due to the internal pressure and the transverse load, the tube has tensile stress between σ_m and σ_0. As the bending moment increases, a portion of the tube may reach zero stress because the membrane cannot resist any compressive force. The zero-stress portion of the tube is denoted by angle θ_0. In this paper, the failure of the structure is defined when $\theta_0 > 0$, which represents the onset of wrinkling.

Wrinkle length is the length of the tube at which wrinkling first occurs for a given loading and geometric conditions. This length depends on the moment necessary to initiate wrinkling. For a given angle θ_0, Comer and Levy (1963) first determined the magnitude of the maximum stress from the balance of the longitudinal forces:

$$\sigma_\mathrm{m} = \frac{\pi pr(1 + \cos\theta_0)}{2t[\sin\theta_0 + (\pi - \theta_0)\cdot\cos\theta_0]}, \tag{3}$$

where r and t are the radius and the thickness of the tube, respectively, and p represents the internal pressure present in the tube. Since bending stress is generated due to the bending moment, the maximum stress can also be expressed in terms of the bending moment M as

$$\sigma_\mathrm{m} = \frac{2M(1 + \cos\theta_0)}{tr^2(2\pi - 2\theta_0 + \sin 2\theta_0)}. \tag{4}$$

By combining these two equations and using the failure criterion of $\theta_0 = 0$, the bending moment necessary to initiate wrinkling can be obtained as:

$$M = \frac{p\pi r^3}{2}. \tag{5}$$

When a constantly distributed force (caused by drag) is applied, the maximum bending moment occurs in the middle of the length. By equating the maximum bending moment with Eq. (5), we have:

$$M_{\max} = \frac{wL^2}{8} = \frac{p\pi r^3}{2}. \tag{6}$$

Solving for L and setting the load, $w = F/L$, yields the general expression for wrinkle length as:

$$L_{\mathrm{wr}} = \frac{4\,p\pi r^3}{F}. \tag{7}$$

The wrinkle length is the length at which wrinkling first occurs in an inflated tube subject to bending, for a given pressure and flow rate. As expected, the wrinkle length will be reduced for a higher loading force, F, and is proportional to the internal pressure and the tube radius. The tube radius, r, is the largest contributing factor to the wrinkle length for these conditions.

For this specific application, the loading force, F, is the drag force, F_{drag}. Since drag force is a function of tube length, Eq. (7) is further expanded using Eq. (9), as:

$$L_{\mathrm{wr}} = \frac{2r}{V}\sqrt{\frac{\pi p}{\rho C_{\mathrm{D}}}}. \tag{8}$$

Eq. (8) now shows the wrinkle length as a function of the core contributing variables for this application, internal pressure, tube radius, and external fluid velocity. The wrinkle lengths defined in Eqs. (7) and (8) depend on the boundary conditions and are derived for the simply-supported conditions shown in Fig. 2.

3. Verification for finite element model

A verification model is first made to explore and verify the finite element membrane analysis for an inflatable tube subject to bending. Once the approach is validated, a full-scale cage will then be modeled to explore the interaction of all the components and system integrity (see Section 5). The verification model is a simply-supported tubular beam with a distributed load and an internal pressure as shown in Fig. 2.

A commercial program, ANSYS (ANSYS Inc., 2004), is used for finite element modeling and simulation in this paper. The verification model is composed of the inflatable tube and two rigid end-caps. Fifty elements along the beam span and 24 elements around the circumference are created. A membrane element (SHELL41 in ANSYS) is used with tensile stiffness, but no compressive stiffness, meeting the tension-only requirements of a fabric material. It is observed that the zero-compressive stiffness caused a numerical instability in the solution of a pressurized beam in bending. Equivalent-geometry shell elements (SHELL63 in ANSYS) with small elastic modulus are merged to the membrane

elements to improve stability of the membrane elements. A high modulus is used for the cap in order to make it rigid compared to the fabric material.

The internal pressure is broken up into pressure acting in the radial direction and pressure acting in the longitudinal direction. The radial pressure is applied normally to the membrane using the surface pressure command (SFE in ANSYS). The longitudinal pressure is converted to the equivalent nodal forces along the circumference of the cap, assuming the cap is rigid. A simply-supported boundary condition is imposed by fixing those nodes on the neutral axis of the cap. The drag force caused by fluid is calculated using Eq. (9) and applied to the tube as a distributed load.

Due to the tension-only behavior of the membrane, the problem is nonlinear and Newton–Raphson iterative method is utilized to solve the nonlinear finite element equations. In order to improve the convergence of the problem, the total load is divided by five sub-steps and the solution is calculated incrementally. When the wrinkling occurs, the structure experiences the rigid body motion and the system matrix has a singularity, which terminates the program.

Simulation results are compared to the theoretical deflection solutions in Section 2. The results for the deflection predicted at the midpoint of a 10 m long tube are shown in Fig. 3. Since flow velocity is proportional to the drag force, flow velocity is used to compare models. The difference between the theoretical and finite element simulation results is 0.567%. These results show that the finite element simulation accurately estimates the behavior of the inflatable structure.

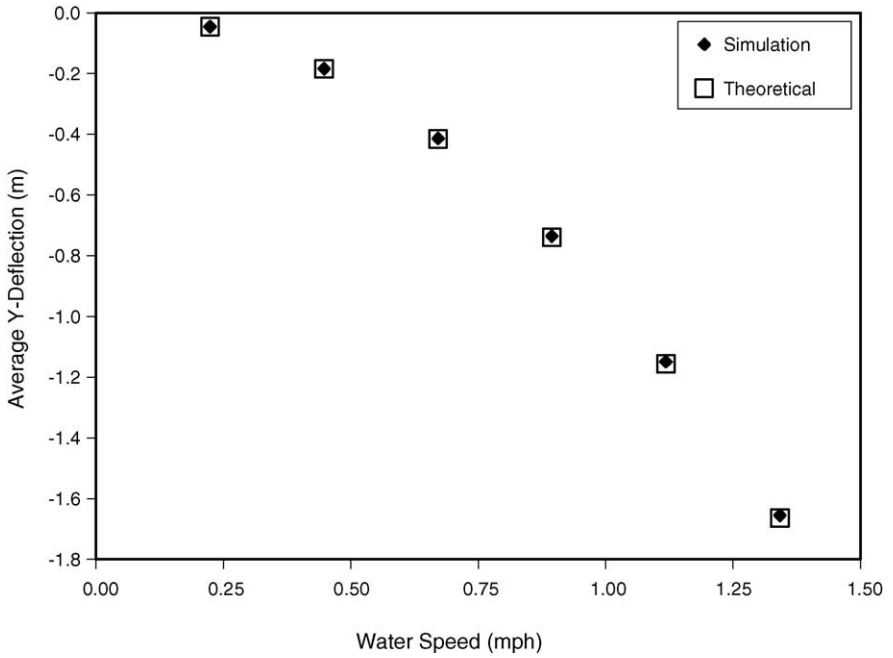

Fig. 3. Deflection results for the verification model with a length of 10 m.

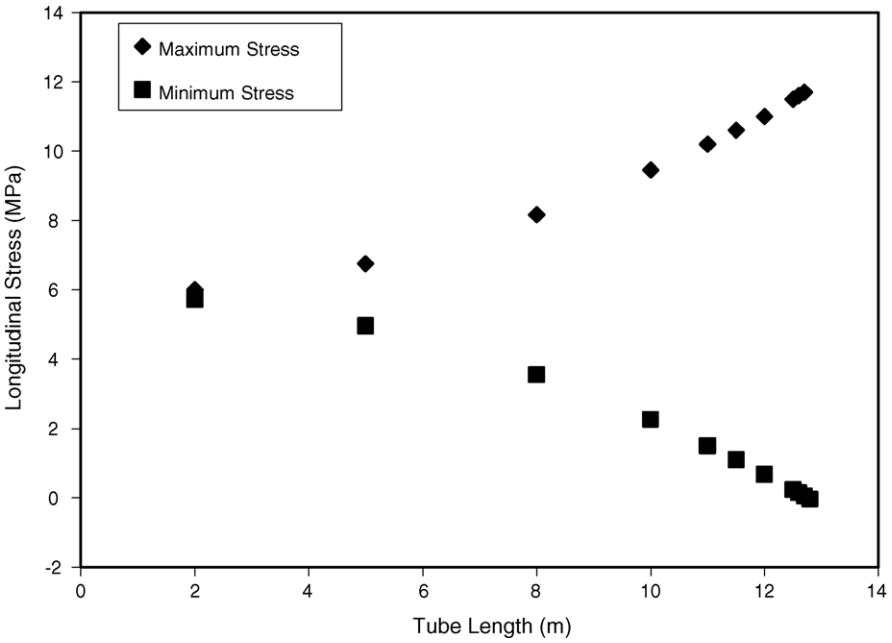

Fig. 4. Longitudinal bending stress results for verification model with 0.5 m/s flow velocity.

Fig. 4 shows the corresponding longitudinal stress results to verify the behavior of the finite element model. As expected, the maximum stress increases, while the minimum stress decreases in bending. A rigid body motion occurs when the minimum longitudinal stress decreases to approximately zero, verifying the tension-only behavior of the model. This defines the failure by wrinkling in this model. The results from the verification model show the merged membrane-shell elements acceptably model the tension-only tubing material.

4. Material properties

Commercially available discharge hose (Kuriyama of America Inc., 2003) is used in this paper as the inflatable material for the preliminary analysis. These tubes are a composite fabric comprised of a combination of molded PVC layers and synthetic fibers. Material properties are anisotropic due to the two fiber layers running $+30^\circ$ and -30° from the longitudinal fibers. The material properties required for the analysis, elastic modulus and Poisson's ratio, are modeled as orthotropic because stresses in the hoop and longitudinal directions are the primary interest. The elastic modulus is determined experimentally, while Poisson's ratio is approximated through simulation.

Samples were cut from the tube in longitudinal and hoop directions as shown in Fig. 5 to determine properties in these directions. Fig. 5 also shows the cross-sectional shape of the tensile specimen with the center section designed to taper from the grip area to a narrow

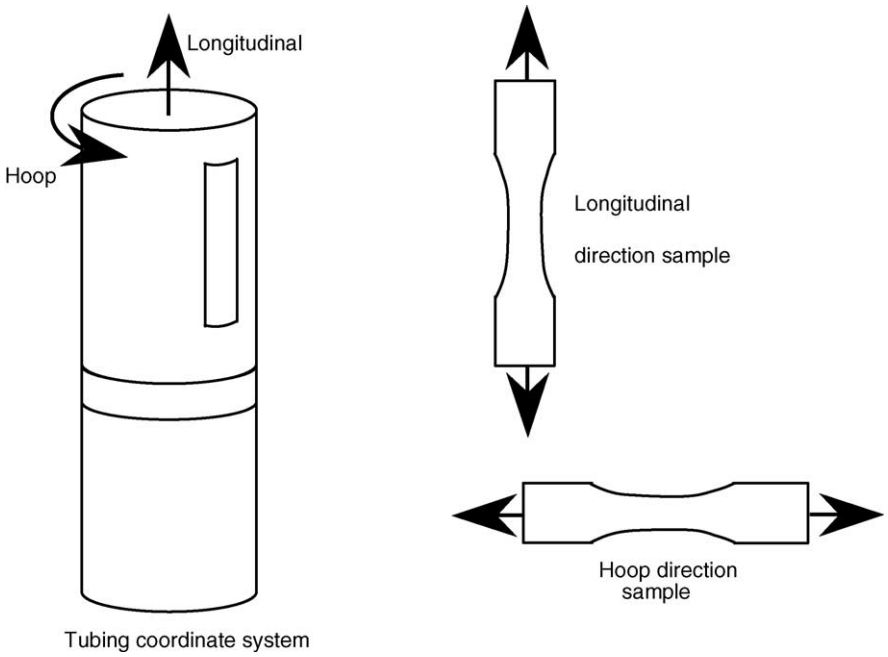

Fig. 5. Test sample orientations with respect to continuous tubing.

strip to control the break location. All specimens are 23 cm long and 2 cm wide at the narrowest section. Since continuous fibers that form the structure of the full fabric tube are severed in the cut samples, a multiplicative correction factor is applied to all tests made from the cut specimens. The correction factor is defined as a ratio of the elastic modulus of an uncut, continuous tube sample to the elastic modulus of a cut specimen. This correction factor of 1.29, obtained from experiment, is applied to all experimental results, including both the longitudinal and hoop-oriented specimens.

An MTI 25k screw-driving tensile test machine was used with Curtis 30k jaw grips to perform the tensile tests. An Interface 1220AF-25k load cell was used in conjunction with MTI software to measure force. After observing preliminary tests, a test speed of 0.10 in./min was considered reasonable and chosen for all tests.

Samples are locked in the test grips and pulled at a test speed of 0.10 in./min until failure. Strain is determined by measuring the distance between marks on the surface of the specimen. Tensile force is measured by a load cell and converted to axial stress using the cross-sectional area of the specimen. A summary of the experimentally measured elastic moduli and corrected orthotropic elastic moduli for the hoop and longitudinal orientations are shown in Table 1.

Due to the nature of the cross-hatched fabric material, in-plane and out-of-plane shape distortions occurred in samples when loaded under tension. The in-plane distortions can be described as uneven shifting of the material in the pull direction. The strain measurements were largely affected by the in-plane distortion because the measurement lines did not remain perpendicular to the sample length. The out-of-plane distortions can be described as

Table 1
Summary of experimental and corrected material properties

Material/orientation	Experimental elastic modulus (psi)	Corrected modulus (psi)
VF 600/hoop	5798.4	7479.9
VF 600/longitudinal	36098.0	46566.4

cupping of the flat, rectangular cross-sectional area. These largely affected the width and, in some cases, thickness measurements. Thus, the measurements for the Poisson's ratio are not reliable. Instead of measuring the Poisson's ratio, a set of finite element simulations are performed by changing the values of the Poisson's ratio. Simulation results show that varying Poisson's ratio had negligible effect on longitudinal stress and deflection. The small variation in stress and deflection justifies assuming a reasonable value of 0.4 for Poisson's ratio.

5. Finite element modeling

5.1. Geometric modeling

There exist an infinite number of directions that current may flow for an underwater cage, however top-down and side flows are most likely to occur. The number of modeled choices is, therefore limited to cages subject to top-down and side flows. Figs. 6 and 7 show an example of each case. All tubes are meshed with merged shell and tension-only membrane elements in the same merged element configuration as the verification model. The tubular connectors in the cage are modeled with high-stiffness shell elements that simulate a rigid body. String elements (LINK10 in ANSYS) are used to model the tension-only cables that tie together certain connectors throughout the cage. Total drag loading is divided equally among nodes and applied as a vector force in the direction of flow. ANSYS

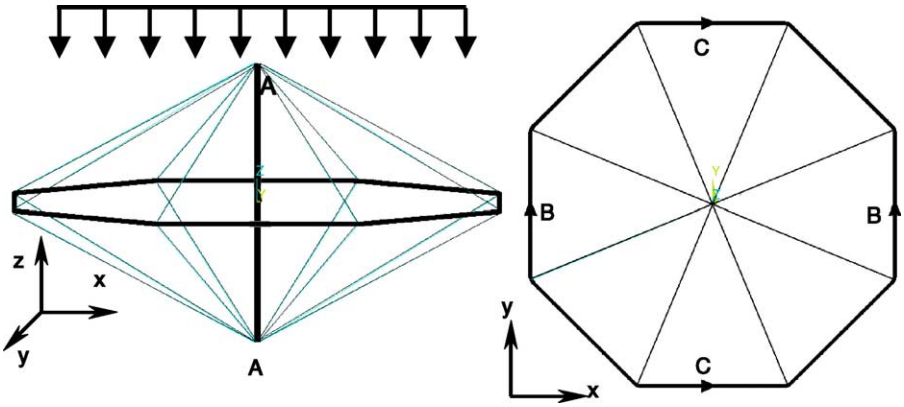

Fig. 6. Top-flow boundary condition locations.

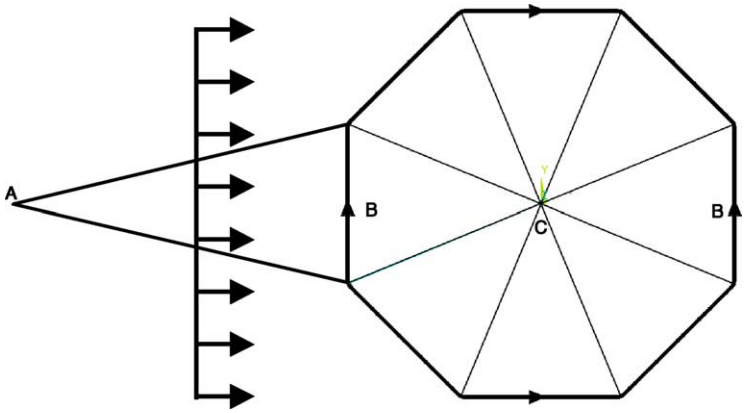

Fig. 7. Side-flow boundary condition locations.

script files are used to parameterize the variables involved in the construction and analysis of each cage so that different designs can easily be obtained by changing these parameters.

Drag on a given member is a direct function of tube length, tube diameter, and the flowing fluid velocity squared. Table 2 presents vinyl-flow data including tube diameter, thickness, and working pressure for a given series number. These three independent variables are combined using data from commercially available materials. The VF Series is then grouped by pressure range to show approximately constant pressure trends.

5.2. Fluid-flow modeling

Flowing water current acting on the cage initiates bending in the inflated members. The flow is assumed to be steady cross-flow over a smooth cylinder. Eq. (9) defines the drag

Table 2
Manufacturer data for vinyl-flow commercial drainage tubing

Series no.	Tube diameter (in.)	Approximate wall thickness (in.)	Working pressures (psi)	Pressure group (psi)
VF 150	1.673	0.0669	80	70–80
VF 200	2.165	0.0669	80	
VF 250	2.598	0.0787	80	
VF 300	3.130	0.0787	70	
VF 400	4.134	0.0827	70	
VF 500	5.039	0.0866	40	40–50
VF 600	6.181	0.0866	50	
VF 800	8.169	0.1063	45	
VF 1000	10.118	0.1181	35	30–35
VF 1200	12.126	0.1181	30	
VF 1400	14.134	0.1181	30	
VF 1600	16.142	0.1181	30	

force, F_{drag}, on a cylinder as a function of tube cross-sectional area, A, drag coefficient, C_D, external fluid density, ρ, and external flow velocity, V.

$$F_{drag} = \frac{1}{2} C_D A \rho V^2 \tag{9}$$

In order to simplify the analysis condition, we assume that (a) smooth cylinder surface, (b) constant temperature of 20 °C, (c) steady-state flow, and (d) constant cross-sectional area. Under these conditions, the coefficient of drag, C_D, can be determined using the Reynold's number. When the Reynold's number is in the range of $10{,}000 \leq Re \leq 200{,}000$, the coefficient of drag is about one (Fox and McDonald, 1998).

5.3. Boundary and load conditions for top-flow simulation

The two locations labeled A in Fig. 6 describe two single nodes at the top and bottom of the cage. Both points are constrained to zero deflection in the x, y, and z directions. The cage diameter-to-height ratio is set to 8:5 in order to emulate the geometry of some commercially existing cages. Cables on the underside of the cage are slack and do not affect the system for this loading case, but were included for aesthetics along with the fixed node at the bottom of the cage.

Locations labeled B and C in Fig. 6 describe all nodes around the circumference of the tube at the center of its length. Nodes at location B are constrained to zero deflection in the y direction. Nodes at location C are constrained to zero deflection in the x direction. Constraining locations B and C prevents rotational rigid body motion while allowing the individual tubes and cage to expand symmetrically.

A main load condition is the drag force caused by flow of the surrounding fluid. Even if the dynamic drag force can be calculated using fluid dynamic models, a simple static force is applied. The justification is that the flow is laminar and the goal is to identify the strength of the inflatable structure. For a given water velocity and the geometry of the cage, the drag force is calculated using Eq. (9) and applied to each member within the structure evenly.

5.4. Boundary and load conditions for side-flow simulation

The location labeled A in Fig. 7 describes the single-node anchor point fixed to zero deflection in the x, y and z directions. To allow symmetric expansion and prevent rotational rigid body motion, constraints are placed in two more locations in the cage. Locations labeled B and C in Fig. 7 describe all nodes around the circumference of a tube at the center of its length. The nodes at location B are constrained to zero deflection in the y direction, while nodes at location C are fixed to zero deflection in the z direction.

5.5. Design criteria

For both flow cases failure occurs when wrinkling exists anywhere in the fabric tubing or when stress exceeds the ultimate strength of the material. Wrinkling is defined as an onset of compressive bending stress. Wrinkling is expected to occur in the longitudinal direction because the combined loading of internal pressure and bending decreases the longitudinal

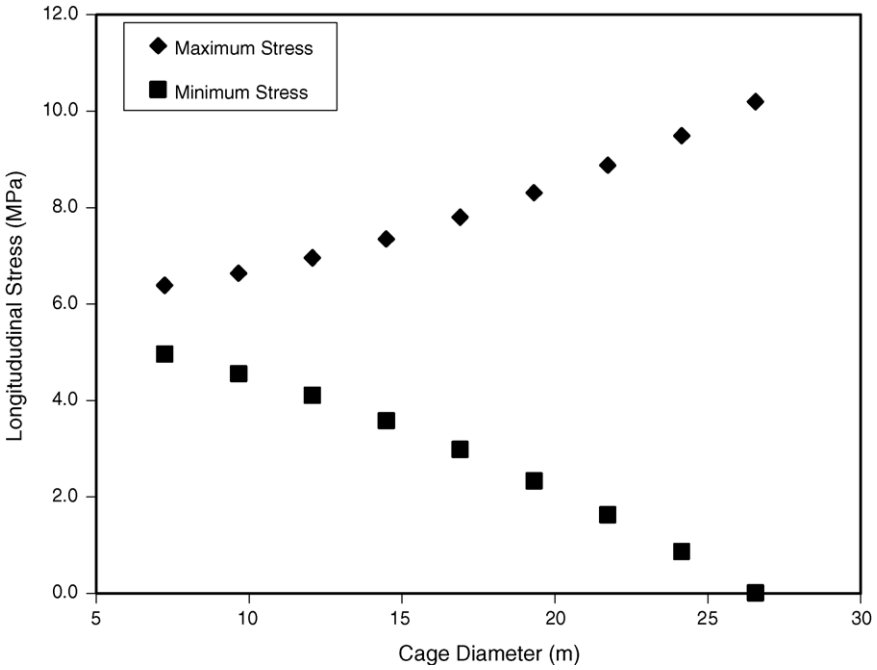

Fig. 8. Simulation results: bending stresses in a VF 800 top-flow cage at 1 knot (1.15 mph).

stress. Tubes are not expected to wrinkle in the hoop direction because the only loading affecting the hoop stress, internal pressure, creates a tensile hoop stress. The maximum stress will occur in the longitudinal direction because the combined loading of internal pressure and bending increase the longitudinal stress. Since the hoop stress is affected only by the internal pressure loading, using the manufacturer's recommended working pressure ensures the hoop stress will not exceed the ultimate strength of the material.

Fig. 8 illustrates a representative case of compressive failure behavior for VF 800 tested at a water speed of 1.0 knot (1.15 mph or 0.514 m/s) in the top-flow direction. Maximum and minimum longitudinal stresses are shown for various cage sizes. As the cage size is increased, maximum stress increases, while minimum stress decreases. Pretension in the tubes keeps both stresses positive, meaning they are always in tension. When the cage size increases to the point that the minimum stress drops below zero, the model fails because the tension-only elements can not support compressive stress. This is then interpreted by the program as an unconstrained model and results in a rigid body motion. Note that the compressive stress could go very slightly negative without failure because of the small compressive strength provided by the merged shell elements comprising the tube.

The side-flow simulations do not show a smooth trend in the longitudinal stress down to zero as in Fig. 8, but show a sudden drop-off resulting in a rigid body motion. This behavior can be described as a buckling of the structural tubes. The stress behavior is due to changes in the higher order bending occurring in the tubes as the cage size changes. This behavior is further explained in Section 6.2.

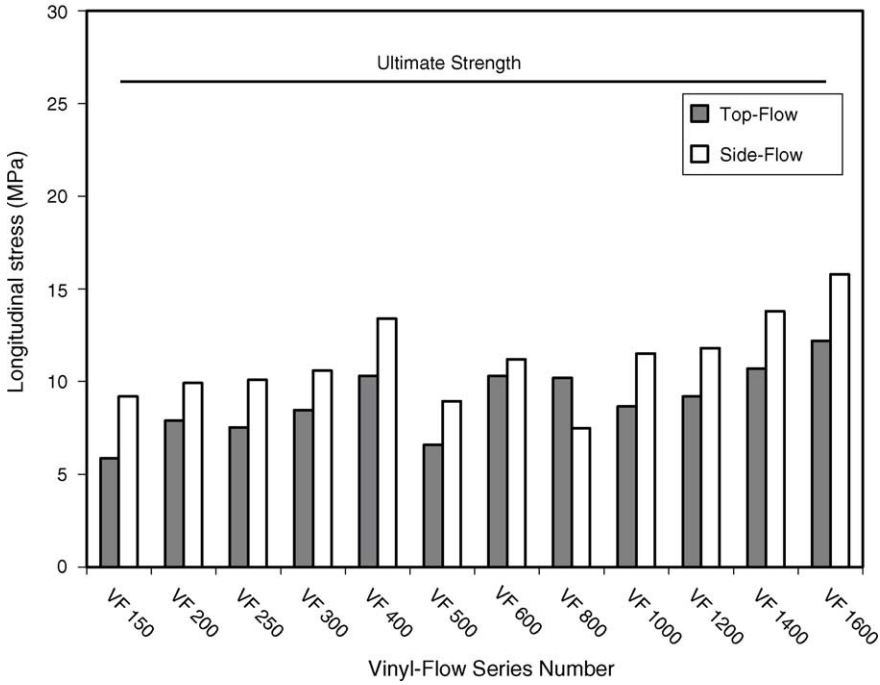

Fig. 9. Maximum stresses in each simulation and ultimate material strength.

6. Results

Twelve commercially available flexible tubes, as listed in Table 2, are tested under top- and side-flow conditions. The design yielding the largest cage is chosen and subject to an additional velocity simulation.

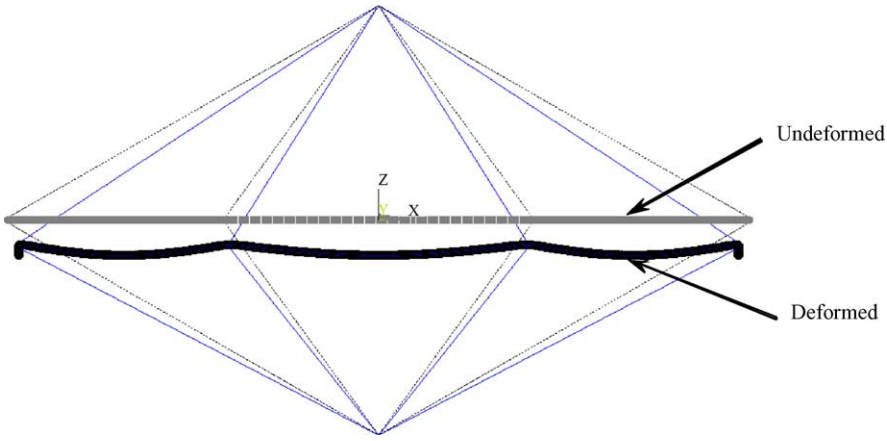

Fig. 10. Top-flow deformed geometry at the wrinkle point.

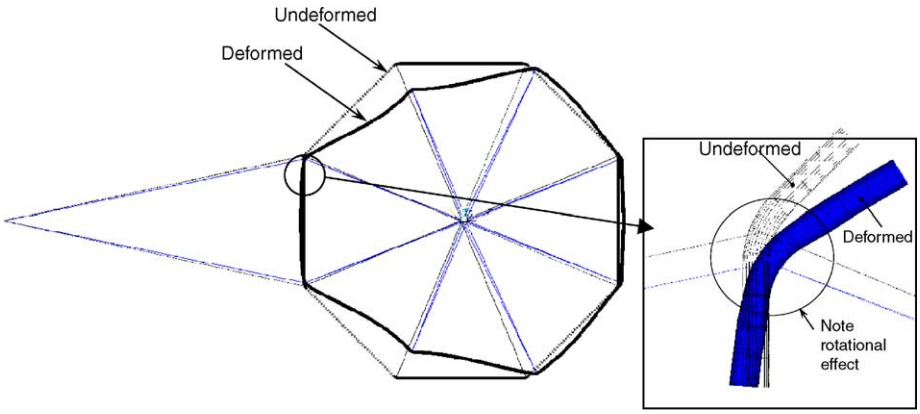

Fig. 11. Side-flow deformed geometry at the wrinkle point.

6.1. Stress results

Fig. 9 illustrates the maximum longitudinal stresses occurring in each simulation staying below the experimentally determined ultimate strength of the material, 26 MPa. This ensures the material strength is not exceeded in any simulation.

6.2. Deformation results

Fig. 10 shows a typical deformed geometry of a cage subject to top flow at the critical wrinkle point. All eight tubes bend in the negative z direction with maximum z deflection occurring at half the tube length. Bending plus the Poisson effect cause the cage diameter to decrease symmetrically throughout the cage.

Table 3
Maximum cage deflections for the top-flow orientation, 1 knot water flow

Series no.	Tube diameter (in.)	Working pressures (psi)	Maximum cage diameter (m)	Ratio of change in x diameter to original cage diameter (%)	Ratio of z deflection to original cage diameter (%)
VF 150	1.673	80	7.2	−4.93	−10.78
VF 200	2.165	80	9.6	−6.49	−14.98
VF 250	2.598	80	10.8	−6.49	−13.53
VF 300	3.130	70	13.2	−7.02	−15.83
VF 400	4.134	70	16.8	−8.71	−18.78
VF 500	5.039	40	14.4	−5.80	−10.57
VF 600	6.181	50	20.4	−8.83	−17.37
VF 800	8.169	45	26.4	−8.75	−17.47
VF 1000	10.118	35	27.6	−7.78	−13.82
VF 1200	12.126	30	30	−7.60	−13.59
VF 1400	14.134	30	34.8	−8.85	−15.76
VF 1600	16.142	30	39.6	−10.10	−17.92

Table 4
Maximum cage deflections for the side-flow orientation, 1 knot water flow

Series no.	Tube diameter (in.)	Working pressure (psi)	Maximum cage diameter (m)	Ratio of change in x diameter to original cage diameter (%)	Ratio of change in y diameter to original cage diameter (%)
VF 150	1.673	80	14.4	2.498	−17.346
VF 200	2.165	80	18	2.600	−18.633
VF 250	2.598	80	20.4	2.598	−18.216
VF 300	3.130	70	21.6	2.681	−18.361
VF 400	4.134	70	27.6	3.138	−21.377
VF 500	5.039	40	18	2.569	−14.222
VF 600	6.181	50	21.6	2.731	−17.667
VF 800	8.169	45	25.2	3.150	−18.619
VF 1000	10.118	35	24	2.672	−15.442
VF 1200	12.126	30	25.2	2.779	−14.976
VF 1400	14.134	30	28.8	3.262	−17.278
VF 1600	16.142	30	32.4	3.760	−19.605

Fig. 11 shows a typical-deformed geometry of a cage subject to side flow at the critical wrinkle point. Note that the net cage x diameter increases, while the net cage y diameter decreases. Internal reaction forces occurring through the cable connections cause internal bending moments around the corner connectors of the octagon. Deformation effects of these internal bending moments are visible in the deformed curvature around the

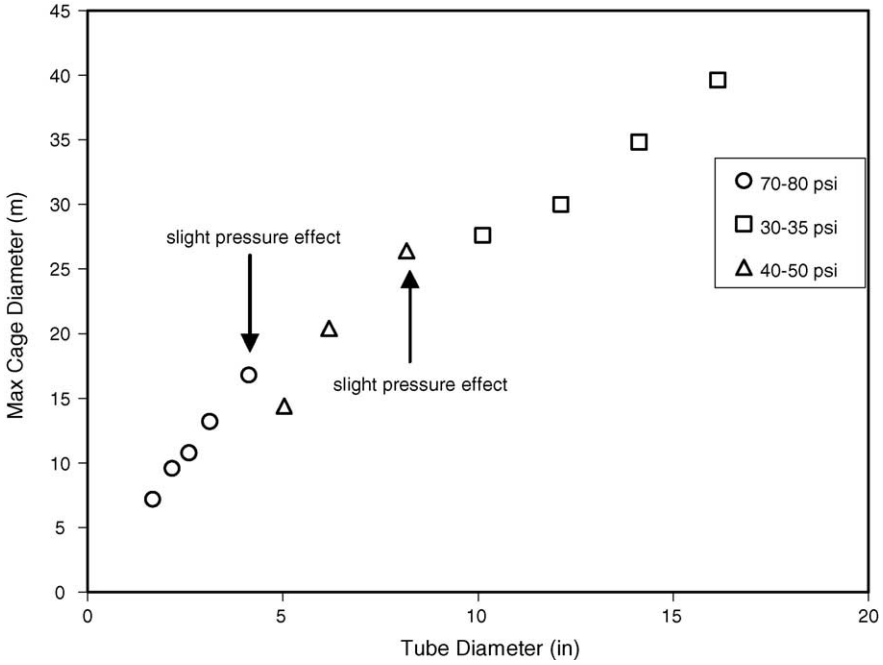

Fig. 12. Top-flow maximum cage diameters for each tubing material grouped by internal pressure.

connectors and account for multiple-mode bending visible in several of the beams. Fig. 11 also illustrates the rotational effect on a representative rigid connector. The different rotational effects occurring throughout the cage contribute to the multiple-bending modes and subsequent buckling stress behavior leading to failure.

Two tables are shown to present deflection behavior with respect to the original cage size. Data are summarized in tabular format because in each case, the maximum deflections occur at different cage sizes which correspond to different drag loadings. With different drag loadings, each case cannot be directly compared to determine a graphical trend. The sign convention for percent changes in deflection is based on direction and follows the previously defined coordinate system. Tube diameter and working pressure are included in the tables for comparison between cases. Table 3 shows the maximum diameter change and maximum z deflection with respect to original cage diameter for the top-flow case. Diameter deflections are between 4 and 10%, while z deflections are between 10 and 18%. Table 4 shows the maximum change in the x and y diameters with respect to original cage diameter for the side-flow case. The magnitudes of x diameter deflections are small and between 2 and 4%, while y deflections are much larger, at 14–22%.

6.3. Parameter study in cage size

The maximum possible cage size is determined by the point at which the cage wrinkles. Figs. 12 and 13 show the maximum cage diameter results by tube diameter for the top-flow

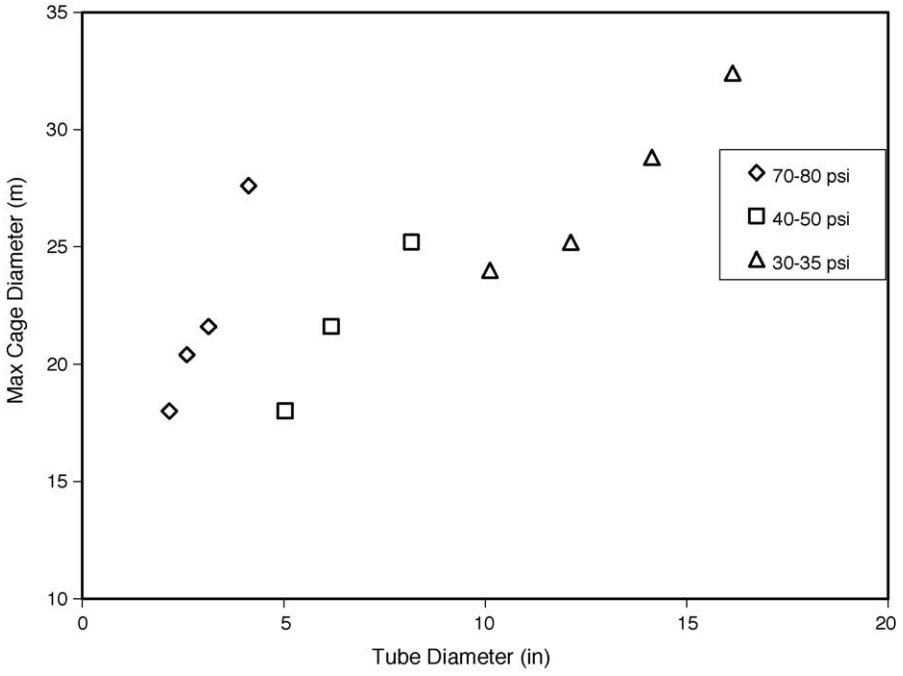

Fig. 13. Side-flow maximum cage diameters for each tubing material grouped by internal pressure.

and side-flow cases, respectively. Slight pressure effects are noted between the pressure groups of the top-flow case, but are neglected to form one linear increasing trend. The trend generally shows that, independent of pressure, as diameter increases, the maximum possible cage diameter increases for top-flow conditions. The side-flow case, however, has significant pressure effects visible in Fig. 13. Each pressure group is plotted with an increasing linear trend, but a distinct slope and *y*-intercept. Within each pressure group, as diameter increases, the maximum possible cage diameter increases. Also evident is that as pressure increases, the slope of the constant pressure trends becomes steeper. This indicates that for a given diameter, operating at higher pressures increases the maximum possible cage size.

Since the flow situations are idealized and true water conditions vary no matter how the cage is anchored, choosing the material for the largest cage is based on the results of both flow cases. Fig. 14 presents the data from Figs. 12 and 13 as a summary of the top-flow and side-flow maximum cage diameters possible for all the material models tested. The maximum size of the cage is determined by the smaller value from the two flow cases. Refer to Table 2 for model specific manufacturer data including tube diameter, thickness, and working pressure for each case.

6.4. Parameter study in velocity

It is also desirable to study how a particular cage is able to withstand water currents higher than 1 knot. The VF 1600 material is chosen because it generated the largest cage

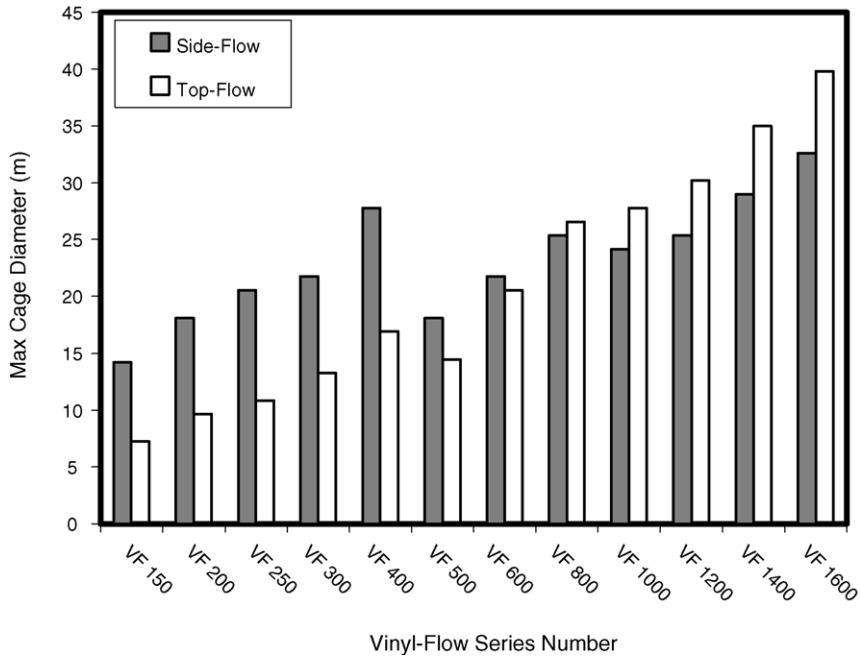

Fig. 14. Summary of maximum possible cage size for each material in two flow cases subject to one knot flow velocity—VF Series number corresponds to the diameter, working pressure, and thickness in Table 2.

size of the various materials tested for 1 knot water flow. The maximum possible VF 1600 cage diameters for top flow and side flow are averaged and then divided by two to obtain an overall cage diameter that is smaller, but able to withstand a higher than one knot flow velocity. A cage diameter of 19.2 m is used for a velocity test on the cage. The flow rate was increased and the cage was able to withstand a maximum flow speed of 1.6 knots in both top and side-flow cases before wrinkling occurred. In top-flow, cage diameter decreases 10.2%, while in side flow, cage x diameter increases 4.0%, and cage y diameter decreases 17.8%. These deflections are reasonable for an inflated flexible membrane cage of this size and correspond to the expected deformation results shown in Section 6.2.

7. Conclusions and discussions

This paper presented a numerical method to model the nonlinear-inflatable behavior of a fabric material by incorporating the theory of inflatable structures into a finite element model. Preliminary simulations successfully show the inflatable behavior for a full-sized cage with top and side-flow models. The side- and top-flow models behave differently, particularly with respect to the divergence volume. The internal pressure and tube diameter play the largest role in deciding the maximum possible cage diameter prior to wrinkling. Instead of including a safety factor in the final results, the failure criterion was set to the point at which wrinkling occurred in any part of the tube. Inflatable tubes do not actually fail at the point of wrinkling, but can continue past this point. Nonlinear finite element modeling is shown to be an effective tool in analyzing the behavior of these structures.

Preliminary findings warrant further research that models the external netting. Net selection has several biological issues to be addressed such as net biofouling and biologically safe mesh size. Further research is also required to address abrasion during biofouling with pressure washers. Net analysis will potentially require dynamic analysis to model the hydrodynamic interaction between the structural element and the fluid (Tsukrov et al., 2000). Since the cage-divergence volume is an important issue, future work should include at least an approximation of the nets. Further simulation work should also optimize the inflatable-material properties. Optimizing the material's properties and size will potentially offset the increased loading of the nets, making the inflatable aquaculture cage practical and economical.

Acknowledgement

This research is supported by National Collegiate Inventors and Innovators Alliance. This support is gratefully acknowledged.

References

ANSYS Inc., 2004. ANSYS User's Manual, ANSYS Inc., Southpointe, 275 Technology Drive, Canonsburg, PA.
Bathe, K.J., 1996. Finite Element Procedure. Prentice-Hall, NJ.

Bridger, C.J., Costa-Pierce, B.A., Goudey, C.A., Stickney, R.R., Fletcher, K., 2001. Towards the development of socially, economically and environmentally sustainable offshore aquaculture in the Gulf of Mexico. In: Proceedings of the International Triennial Conference & Exposition of Aquaculture, 21–25 January, Lake Buena Vista, FL, p. 81.

Bucklin, A., Howell, H., 1998. Progress and prospects from the University of New Hampshire Open Ocean Aquaculture Demonstration Project. In: Proceedings of the Third International Conference on Open Ocean Aquaculture, 10–15 May, Corpus Christi, TX, pp. 7–30.

Comer, R., Levy, S., 1963. Deflections of an inflated circular-cylindrical cantilever beam. AIAA J. 1, 1652–1655.

Davis, D.A., Arnold, C.R., Holt, G.J., 1998. Research summary on potential mariculture species for the Gulf of Mexico. In: Proceedings of the Third International Conference on Open Ocean Aquaculture, 10–15 May, Corpus Christi, TX, pp. 120–131.

Douglas, W., 1969. Bending stiffness of an inflated cylindrical cantilever beam. AIAA J. 7, 1248–1253.

Fox, R., McDonald, A., 1998. Introduction to Fluid Mechanics. John Wiley & Sons, Inc., New York.

Jenkins, C.M., 2001. Gossamer spacecraft: membrane and inflatable structures technology for space applications. In: Progress in Astronautics and Aeronautics Series, V-191unknown:book, American Institute of Aeronautics and Astronautics, Reston, VA, pp. 103–105.

Kuriyama of America, Inc., 2003. PVC Layflat water discharge hoses, http://www.kuriyama.com/, 1221 Landmeier Rd., Elk Grove Village, IL.

Loverich, G., Forster, J., 2000. Advances in offshore cage design using spar buoys. Mar. Technol. Soc. J. 34, 18–28.

Main, J.A., Perterson, S.W., Straus, A.M., 1994. Load–deflection behavior of space-based inflatable fabric beams. J. Aerospace Eng. 7, 225–238.

Main, J.A., Perterson, S.W., Straus, A.M., 1995. Beam-type bending of space-based inflated membrane structure. J. Aerospace Eng. 8, 120–125.

Sakamoto, H., Natori, M.C., Miyazaki, Y., 2001. Deflection of multi-cellular inflatable tubes for redundant space structures. Paper no. AIAA-2001-1617 In: Proceedings of the 42nd AIAA/ASME/ASCE/AHS/ASC Structures, Structural Dynamics, and Materials Conference and Exhibit, 16–19 April, Seattle, WA.

Topping, A., 1964. Shear deflections and buckling characteristics of inflated members. J. Aircraft 1, 289–293.

Tsukrov, I., Ozbay, M., Fredriksson, D., Swift, M., Baldwin, K., Celikkol, B., 2000. Open ocean aquaculture engineering: numerical modeling. Mar. Technol. Soc. J. 34, 29–40.